ADVANCED OPTICAL MATERIALS
www.advopticalmat.de

Chiral Gold Nanopropellers: Engineering Plasmonic Chirality for Enantioselective Recognition Through Stereoselective Binding

*Muhammad Haroon, Liping Huang, Anwer Hayat, Hongyu Chen, and Xiao You**

Enantioselective sensing remains a challenge due to the weak chiroptical responses of small molecules and the limited stereospecificity of plasmonic substrates. Here, a dual-modality platform that integrates plasmonic chirality and molecular recognition is designed and implemented using cysteine-functionalized chiral gold nanopropellers (CGNPs). The structural chirality of CGNPs creates localized optical hotspots with defined handedness, which are further amplified through the stereoselective binding of chiral ligands. Surface-enhanced Raman spectroscopy (SERS) reveals reproducible intensity enhancements and band shifts for stereomatched CGNP–analyte combinations. Quantitatively, the chiral discrimination ability (CDA) reaches 36.0%, and the detection limit for L-phenylalanine is 2.75 µM. Circular dichroism spectroscopy confirms the selective chiral interactions, while density functional theory (DFT) calculations indicate lower binding energy and shorter interaction distances for the L-CGNP–L-phenylalanine complex. Finite-difference time-domain (FDTD) simulations show that handedness-matched light and nanopropeller geometry yield stronger near-field intensities and more radiative plasmonic modes. These combined experimental and theoretical results demonstrate that enantioselectivity arises from the cooperative effect of chiral field localization and stereospecific molecular adsorption. Together, these results establish CGNPs as a versatile platform for enantioselective sensing, integrating chiral plasmonics and molecular recognition for next-generation analytical technologies.

1. Introduction

Chirality, characterized by molecular asymmetry, profoundly influences chemical interactions in biological and pharmaceutical systems. Enantiomers—mirror-image isomers of chiral molecules—often exhibit distinct physiological behaviors, resulting in dramatically different physiological outcomes. This distinction is particularly critical in pharmacology and toxicology, where even minor enantiomeric imbalances can lead to therapeutic failures or adverse effects.[1,2] A prominent example is the thalidomide tragedy of the 1950s, during which the R-enantiomer of the drug led to over 10000 birth defects, thereby underscoring the vital importance of precise chiral discrimination in the process of drug development.[3,4]

Currently established techniques for enantiomer differentiation include circular dichroism spectroscopy (CD).[5] chiral chromatography,[6,7] nuclear magnetic resonance (NMR),[8,9] and capillary electrophoresis[10,11] Although effective, these methods often involve complex instrumentation, high operational costs, or limited sensitivity. Surface-enhanced Raman spectroscopy (SERS) emerges as an attractive alternative due to its exceptional sensitivity and structural specificity.[12–14] Nonetheless, conventional SERS substrates, typically composed of achiral or symmetric nanostructures, inherently lack the ability to selectively amplify enantioselective molecular interactions.[15–18]

Chiral plasmonic nanostructures, however, offer a promising solution to overcome these limitations. These nanostructures generate localized chiral optical fields that enable control and

M. Haroon, A. Hayat, X. You
School of Engineering
Westlake University
Hangzhou, Zhejiang 310030, China
E-mail: youxiao@westlake.edu.cn
M. Haroon, A. Hayat, X. You
Key Laboratory of Intelligent Low-Carbon Biosynthesis of Zhejiang Province
Westlake University
Hangzhou, Zhejiang 310030, China
L. Huang, H. Chen
Department of Chemistry, School of Science and Key Laboratory for Quantum Materials of Zhejiang Province, Research Center for Industries of the Future
Westlake University
Hangzhou 310030, P. R. China
L. Huang, H. Chen
Institute of Natural Sciences
Westlake Institute for Advanced Study
Hangzhou 310024, P. R. China
The ORCID identification number(s) for the author(s) of this article can be found under https://doi.org/10.1002/adom.202501589

DOI: 10.1002/adom.202501589

enhance enantiospecific light-matter interactions[19–23] Recent advances in seed-mediated, ligand-directed synthesis have allowed precise control over nanostructure chirality,[24–27] resulting in surfaces with intrinsic optical activity capable of amplifying chiral molecular signals.[28] By combining plasmonic signal enhancement with enantiospecific molecular recognition, these materials have the potential to address longstanding challenges in enantioselectivity.

Two primary mechanisms underlie current chiral detection methods: optical interactions based on intrinsic chiroptical properties,[29] and molecular recognition driven by selective host-guest interactions.[30,31] Light-matter interactions utilize the intrinsic optical activity of enantiomers but are often limited by low sensitivity, weak molecular responses, and a lack of structural or interaction-based information.[32,33] Molecular recognition techniques, relying on host-guest interactions (hydrogen bonding, π–π stacking, and hydrophobic effects), are widely employed but often constrained by insufficient signal transduction and environmental sensitivity.[18] For instance, SERS-based systems can integrate chiral gold nanostructures (light-matter interactions) functionalized with host molecules (e.g., cyclodextrins, crown ethers) to selectively capture enantiomers. A hybrid strategy that integrates plasmonic optical enhancement with molecular recognition could significantly advance chiral sensing, improving both sensitivity and specificity.

In this study, we design a chiral sensing platform that integrates chiral gold nanopropellers (CGNPs) with cysteine as a chiral mediator, combining plasmonic chiral fields with enantioselective molecular recognition. The inherent chirality of CGNPs generates localized optical hotspots that amplify enantioselective Raman signals, while cysteine ligands mediate precise molecular interactions through stereoselective binding. This approach addresses the sensitivity and selectivity limitations of current methods by leveraging both optical chirality and stereospecific binding. To elucidate the underlying mechanisms, we employed density functional theory (DFT), finite-difference time-domain (FDTD) simulations, and spectroscopic analyses (CD and Raman spectroscopy). The strategy and mechanistic insights presented here establish a foundation for advancing chiral plasmonic sensing technologies.

2. Results and Discussion

2.1. Design and Chiroptical Characterization of Functionalized Chiral Nanopropellers

The development of an effective enantioselective platform requires the precise engineering of both nanoscale structural chirality and specific molecular recognition sites. To achieve this, we first synthesized chiral gold nanopropellers (CGNPs) via a seed-mediated growth method.[24] Briefly, glutathione (3.6 μM) was used as the chiral ligand with ascorbic acid (8.8 mM) as the reducing agent and CTAB (14.75 mM) as the stabilizer and $HAuCl_4$ (0.37 mM) as the gold precursor. Au decahedral seeds directed the formation of the chiral nanostructures at 30 °C over 2 hours. The purified CGNPs showed colloidal stability for over 7 days when stored at room temperature, as confirmed by UV–vis spectroscopy (Figure S2d, Supporting Information).

The structural integrity and morphology of the CGNPs were confirmed by scanning electron microscopy (SEM), as shown in **Figure 1**a and b. The images reveal the successful fabrication of both L- and D-handed nanopropellers with a uniform, well-defined architecture. These nanostructures feature an average particle diameter of approximately 285 nm and consistent nanoscale groove dimensions of around 9 nm (details in Figure S1, Supporting Information), which are critical for generating their unique plasmonic and chiroptical properties.

The optical response of the bare CGNPs was characterized by UV–vis spectroscopy, which showed a broad plasmon resonance centered at approximately 580 nm (Figure S2c, Supporting Information). This feature is consistent with the complex, anisotropic morphology of the nanopropellers and aligns with the wavelength region used for subsequent chiroptical and SERS experiments.

The intrinsic chirality arising from this engineered geometry was experimentally validated using circular dichroism (CD) spectroscopy. As expected, the L- and D-CGNPs displayed distinct, mirror-image CD signals, confirming their opposite handedness (Figure S2a,b, Supporting Information). A slight asymmetry between the L- and D-spectra is observed, which we attribute to the differing purities of the commercially available L-glutathione (≥98%) versus the custom-synthesized D-glutathione (≥96%). This discrepancy in ligand purity may lead to minor morphological differences between the two enantiomeric nanoparticles. Similar deviations from perfect mirror-image CD spectra have also been reported in previous studies involving GSH-directed synthesis of chiral nanostructures.[34–36] These experimental observations, supported by finite-difference time-domain (FDTD) simulations which predicted distinct g-factors, confirm the successful induction of chirality at the nanoscale within the CGNP framework. The simulated g-factor of CGNPs is higher than the experimental value (around ±0.01), which can be attributed to the structural and morphological heterogeneity of nanoparticles in solution, leading to averaging effects that reduce the ensemble CD response.

To enable stereoselective molecular interactions at the plasmonic surface, the CGNPs were subsequently functionalized with L- and D-cysteine. The covalent attachment of cysteine to the gold surface was verified by Raman spectroscopy (Figure 1c). The disappearance of the S–H stretching band (typically around 2570 cm^{-1}) and the concomitant emergence of an Au–S stretching band (observed at ≈267 cm^{-1}) provided clear evidence of thiol-gold bond formation. Furthermore, a diminished intensity of the S–S stretching mode (513 cm^{-1}) and a discernible redshift in the C–S stretching band (from ≈679 cm^{-1} to 663 cm^{-1}) suggested that cysteine adsorbed as monomers without inducing significant nanostructure aggregation.[37]

The impact of cysteine functionalization on the overall chiroptical properties of the CGNPs was further investigated by CD spectroscopy. Upon cysteine binding, a decrease in CD intensity near 580 nm, accompanied by a new signal around 200 nm, is attributed to ligand-induced surface shielding, minor aggregation effects, and chiral coupling. Such chiral coupling can redistribute the energy of the chiral plasmonic field into molecular energy states of cysteine and contribute to the suppression of the CD signal of CGNPs.[28,38] New CD signatures around 200 nm appeared upon functionalization, with LC-LCGNPs showing

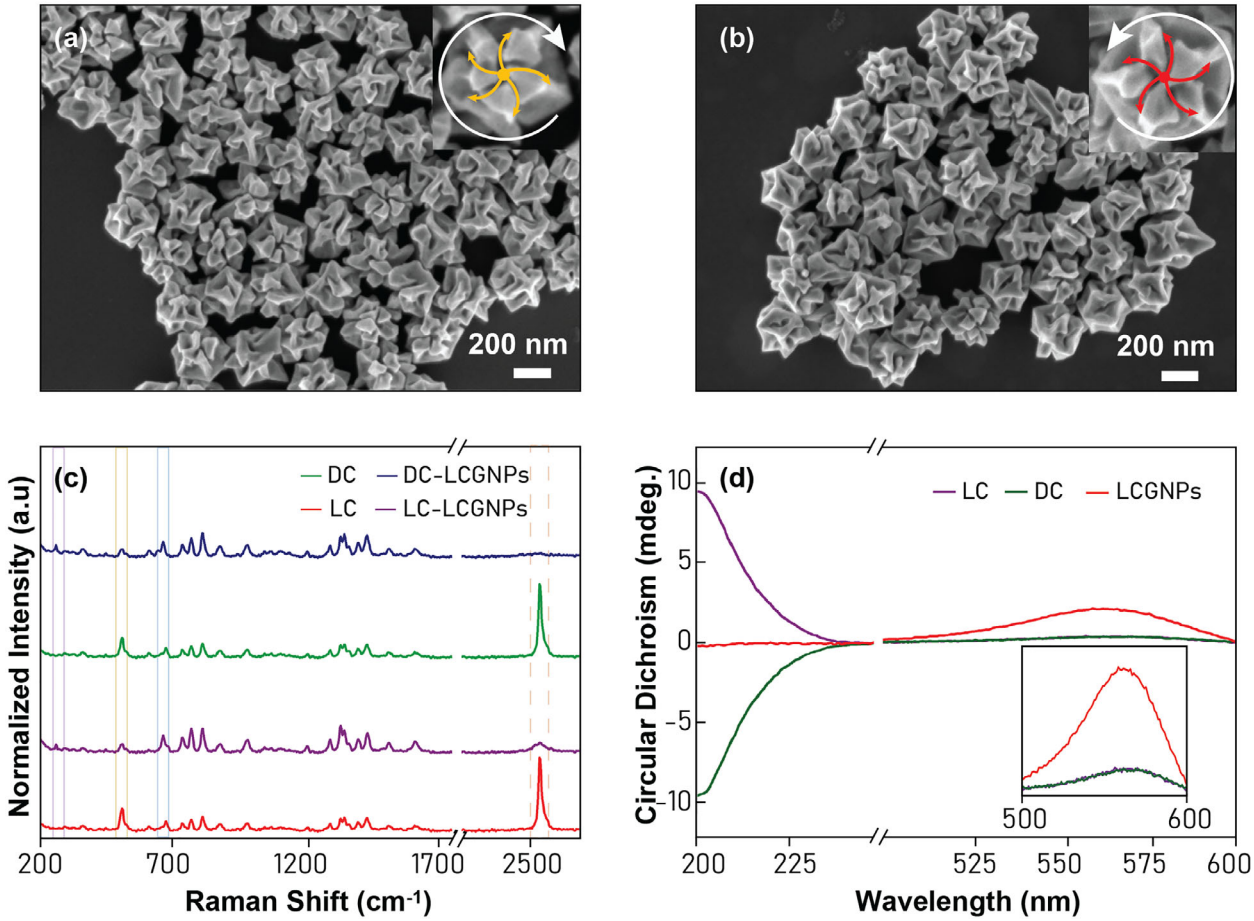

Figure 1. Structural and chiroptical characterization of CGNPs. a,b) SEM images of L- and D-CGNPs, showing well-defined propeller morphologies and consistent structural features with nanoscale chirality highlighted in the insets. c) Raman spectra of pristine and cysteine-functionalized CGNPs, confirming successful thiol binding via Au–S and C–S signatures. d) CD spectra of CGNPs before and after L-/D-cysteine modification, demonstrating enantiospecific optical responses. The inset highlights the effect of functionalization on the chiroptical response of CGNPs.

positive bands and DC-LCGNPs exhibiting corresponding negative signals (Figure 1d). The new CD signals likely originate from electronic transitions intrinsic to the chiral cysteine ligand itself ($\pi \rightarrow \pi$ and $n \rightarrow \pi^*$ transitions), rather than from plasmonic resonances. This assignment is consistent with known chiroptical properties of cysteine in the UV spectral region, clearly reflecting surface modification.

Taken together, the spectroscopic analyses demonstrate effective cysteine-mediated surface functionalization of CGNPs. The Raman data confirm robust Au–S bond formation, while the CD data, in conjunction with the strong SERS performance, indicate that the underlying chiral geometry of the nanopropellers is maintained post-functionalization. These spectroscopic findings align with prior literature reports[30] and demonstrate that chiral geometry and chiral optical activity of CGNPs remain intact, rendering them suitable for subsequent enantioselective studies.

2.2. Enantioselective SERS Detection of Phenylalanine

As a control, conventional Raman spectra were obtained from bulk powders of pure D-phenylalanine (DP) and L-phenylalanine (LP) (Figure S4a, Supporting Information). Both enantiomers produced nearly indistinguishable spectral profiles. Characteristic Raman bands were identified at 1605 cm^{-1} (aromatic ring stretching), 1587 cm^{-1} (C=C bending), 1443 cm^{-1} (CH_2 bending), 1410 cm^{-1} (COO^- symmetric stretching), and 1309 cm^{-1} (NH_2 bending), among other vibrational modes. The high degree of similarity between these spectra underscores the inherent limitation of conventional Raman spectroscopy in differentiating enantiomers directly, thereby highlighting the need for advanced analytical methods that can amplify subtle stereochemical distinctions, such as the SERS approach developed herein. To isolate the role of the chiral ligand, the Control SERS experiments were conducted on the bare LCGNPs interacting with L- and D-phenylalanine. The results (Figure S5, Supporting Information) showed low and variable signal intensities, attributable to weak, non-specific physisorption of the enantiomers on the gold surface. This indicates that the chiral shape alone provides insufficient binding affinity for effective and selective detection.

The SERS performance of cysteine-functionalized CGNPs in enantiomeric discrimination was investigated using L- and D-phenylalanine (LP and DP) as model analytes. SERS spectra were recorded for L-cysteine functionalized L-CGNPs (LC-LCGNPs)

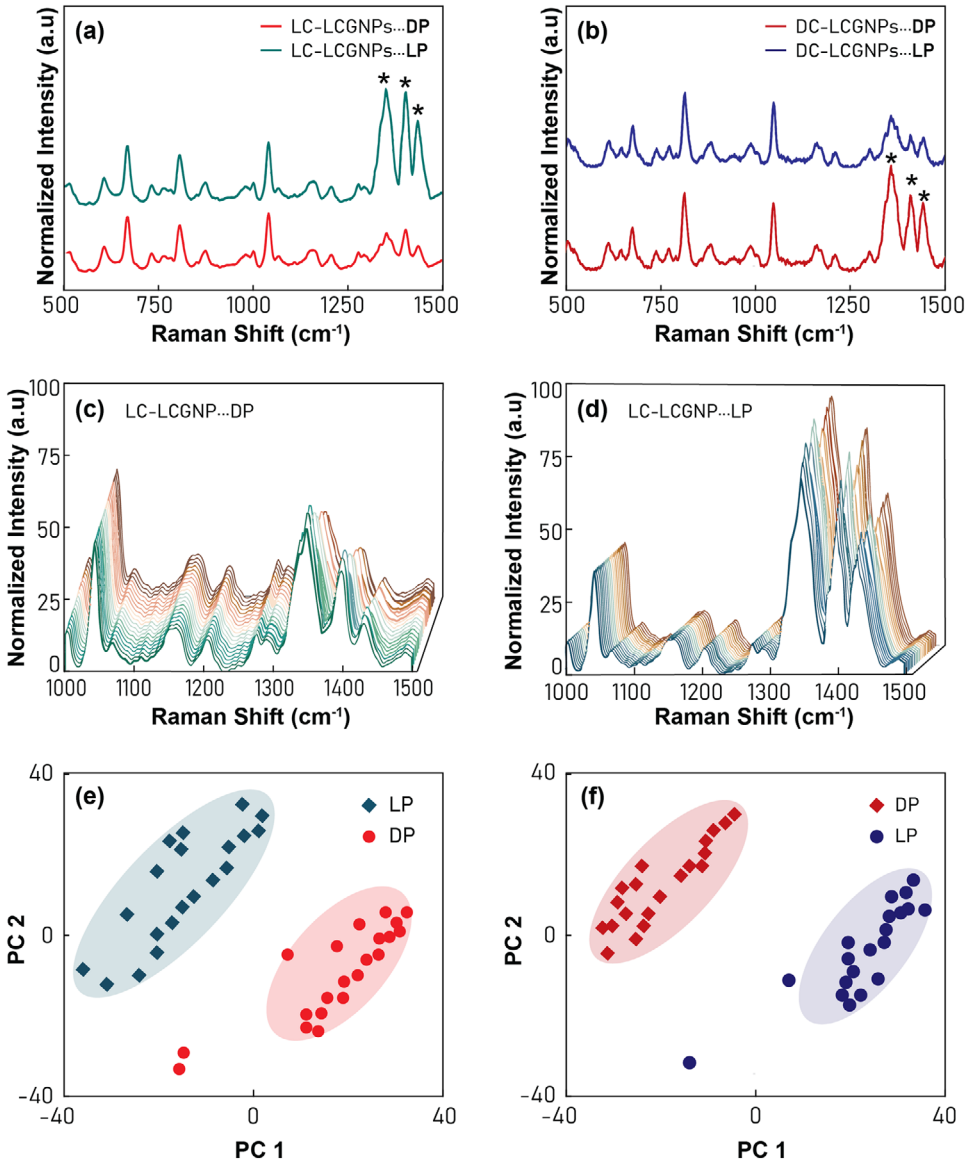

Figure 2. Enantioselective SERS detection of phenylalanine using cysteine-functionalized CGNPs. a,b) SERS spectra of (a) LC-LCGNPs with LP (blue) and DP (red), and (b) DC-LCGNPs with DP (red) and LP (blue); Prominent Raman peaks indicating key vibrational modes are marked (*), highlight enantioselective responses under stereomatched and mismatched configurations c,d) Spectral features across 20 spectra per pairing demonstrates high spectral reproducibility and consistent enantiomer-specific responses e,f) Principal component analysis (PCA) clustering reveals clear spectral clustering between LP and DP, confirming chiral differentiation under stereomatched versus mismatched conditions.

upon interaction with LP and DP (**Figure** 2a). Correspondingly, D-cysteine functionalized D-CGNPs (DC-DCGNPs) were evaluated with LP and DP (Figure 2b). A clear differentiation in SERS signal intensity was observed based on the stereochemical relationship between the functionalized CGNPs and the phenylalanine enantiomer. Specifically, prominent Raman bands of phenylalanine, such as CH_2 bending (≈1346 cm^{-1}), COO^- stretching (≈1400 cm^{-1}), and NH_2 stretching (≈1429 cm^{-1}) exhibited substantially higher intensities when the handedness of the CGNP-cysteine system matched that of the phenylalanine enantiomer (i.e., LC-LCGNPs with LP, DC-DCGNPs with DP). Conversely, interactions involving mismatched handedness (e.g., LC-LCGNPs with DP) yielded significantly attenuated SERS signals for these bands. The consistency of these spectral features and intensity differences was verified through the collection of 20 replicate spectra for each CGNP-analyte pairing, as shown for representative systems in Figure 2c,d.

To provide a quantitative measure of this spectral differentiation, principal component analysis (PCA) was performed on the SERS datasets within the 1000–1500 cm^{-1} spectral window. PCA is a dimensionality-reduction technique that transforms a complex dataset into a new coordinate system. The first principal component (PC1) captures the largest variance in the data, while PC2 captures the second largest. In Figure 2e and f, the distinct, non-overlapping clusters formed by the LP and DP data points confirm that the spectral differences are statistically

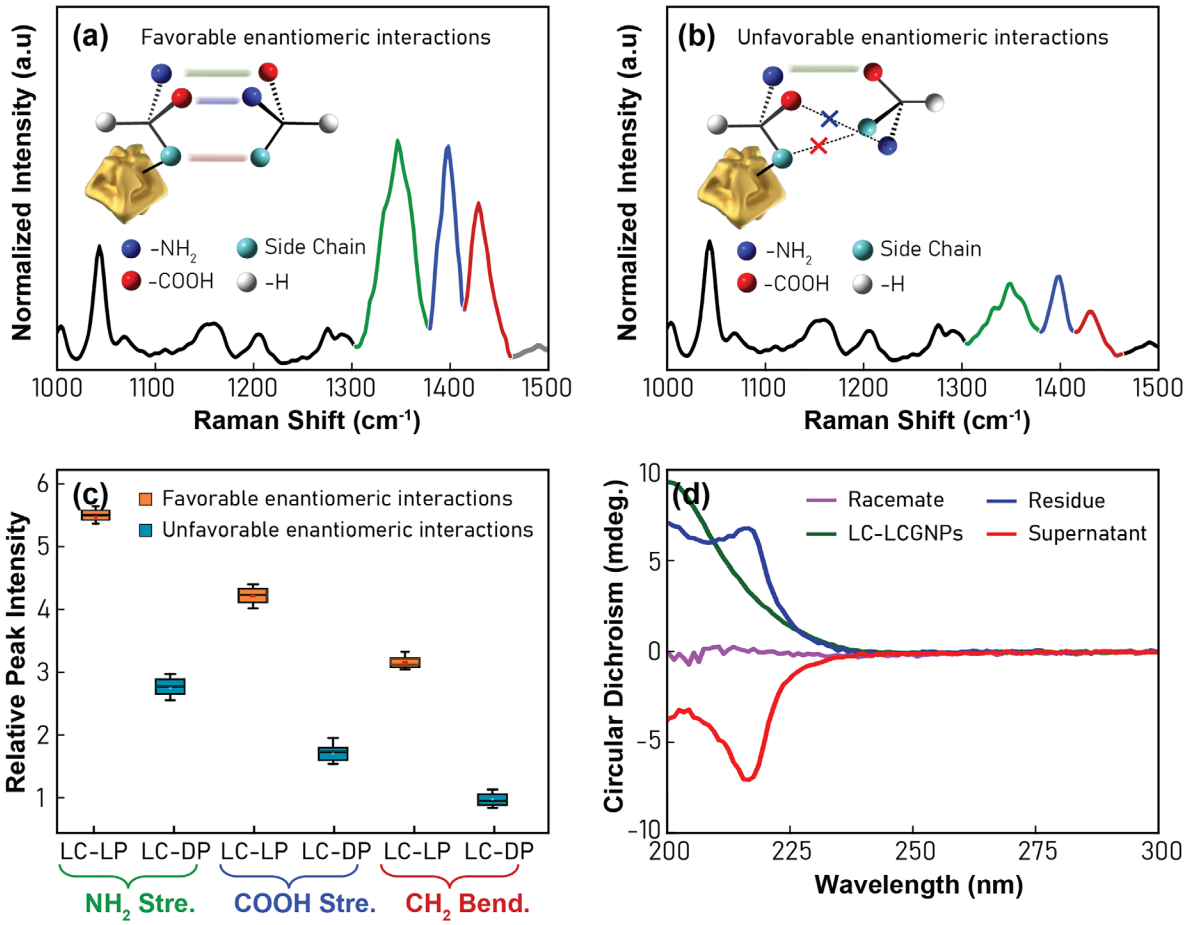

Figure 3. Spectroscopic and theoretical insights into stereoselective interactions. a,b) Raman spectra showing significant relative peak intensity change upon interaction of LC-LCGNPs with (a) LP and (b) DP, including schematic diagrams illustrating key functional groups mediating interactions, color-matched to corresponding Raman bands; c) Boxplot of relative Raman intensities for three key vibrational modes (CH_2 bending, COO^- symmetric stretching, and NH_2 Stretching), comparing LC-CGNPs interactions with L-phenylalanine (LP) (orange) and D-phenylalanine (DP) (violet). The boxplots illustrate the distribution of Raman peak intensities across 20 measurements, indicating preferential binding and enantioselectivity. d) CD spectra of bound and unbound fractions following chiral separation, validating stereoselective capture.

significant. The resulting PCA score plots (Figure 2e,f) demonstrate distinct and well-separated clusters corresponding to stereomatched versus mismatched interactions. For example, analysis of LC-LCGNPs (Figure 2e) showed clear separation between the spectral data obtained from LP and DP. A similar degree of separation was observed for the DC-DCGNP system (Figure 2f). This level of statistical discrimination was not attainable using conventional Raman spectroscopy of the bulk analytes (Figure S4b, Supporting Information). These results directly indicate that the CGNP-based SERS platform, incorporating both engineered plasmonic chirality and a stereoselective interface, enables reliable enantioselective recognition.

2.3. Mechanistic Elucidation of Enantioselective Recognition

2.3.1. Spectroscopic Insights into Chiral Interactions

Detailed examination of Raman band positions upon the interaction of phenylalanine enantiomers with functionalized CGNPs provides insight into the molecular recognition mechanism (**Figure 3**). For instance, when LP interacted with LC-LCGNPs, notable shifts were observed in characteristic Raman bands. The three key Raman bands associated with LC-LCGNPs were observed at 1430 cm^{-1} (CH_2 bending), 1395 cm^{-1} (COO^- symmetric stretching), and 1345 cm^{-1} (NH_2 stretching), while LP exhibited characteristic bands at 1443 cm^{-1}, 1410 cm^{-1}, and 1309 cm^{-1} for the same vibrational modes. Upon interaction of LC-LCGNPs with LP, these bands shifted to 1427 cm^{-1}, 1400 cm^{-1}, and 1348 cm^{-1}, respectively. The vibrational assignments of these prominent Raman bands were confirmed by DFT simulations and supported by the literature (Table S2, Supporting Information). The shifts in these bands are indicative of modifications in the local chemical environment of these functional groups, likely due to hydrogen bonding, electrostatic interactions, and steric effects at the CGNP-cysteine-phenylalanine interface (Figure 3a). The observed Raman shifts in CH_2 bending, COO^- symmetric stretching, and NH_2 stretching are substantial beyond our instrumental spectral resolution (≈1.5 cm^{-1}). These shifts were statistically validated by averaging multiple spectra

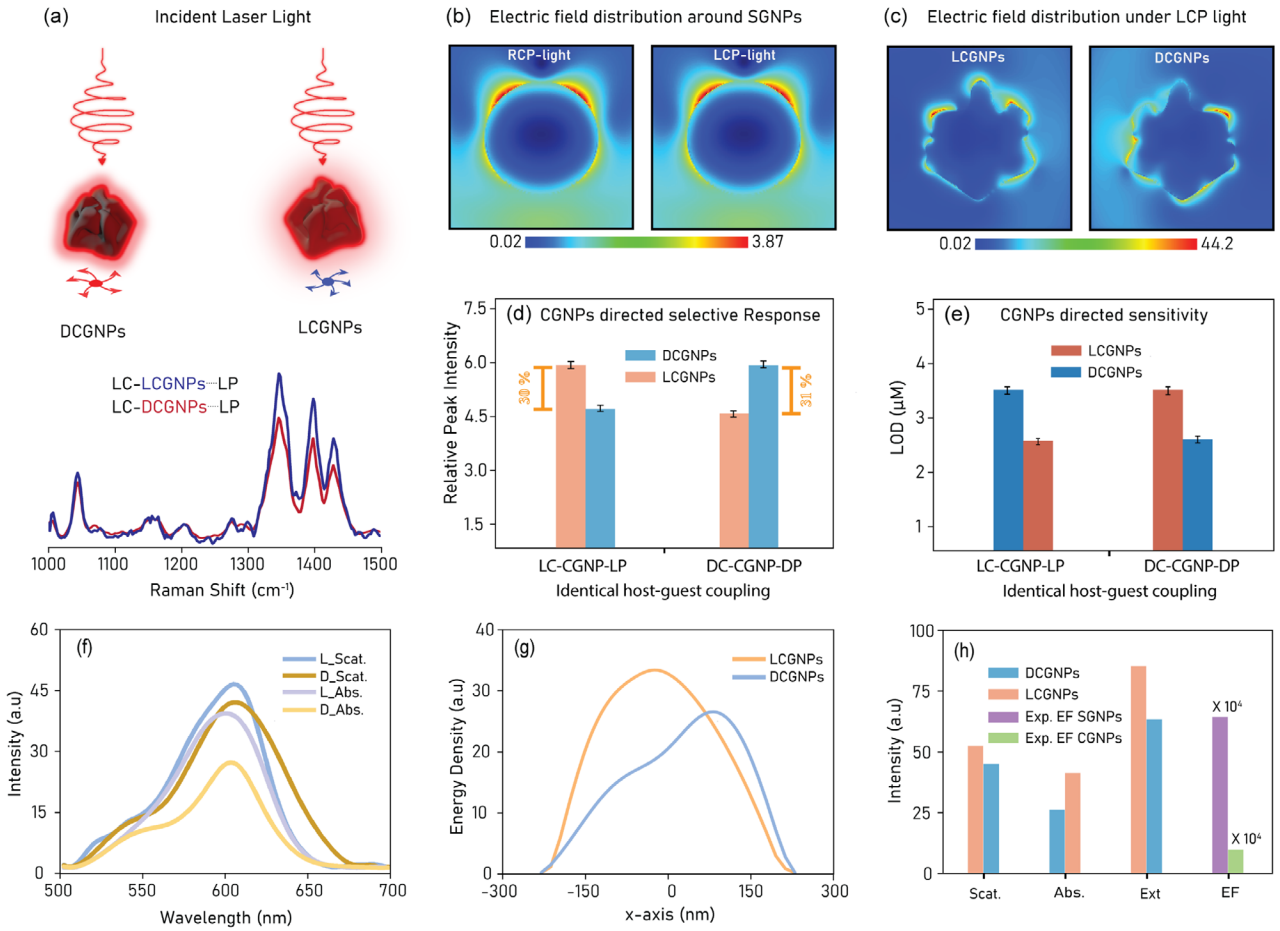

Figure 4. Correlation of optical simulation and experimental SERS enhancement. a) Schematic and Raman spectra showing stronger enhancement under matched chirality. b, c) FDTD-simulated field maps for achiral SGNPs vs. chiral CGNPs under left circularly polarized (LCP) illumination. The field maps show the distribution of the electric field intensity around the nanoparticles, highlighting the stronger and more localized field enhancements around CGNPs due to their chiral geometry. d) Peak intensity comparisons. e) Limits of detection for different chiral pairings. f–h) Simulated scattering, absorption, and energy density plots illustrating enhanced radiative behavior in stereomatched systems.

(n = 20), confirming reproducibility and significance beyond experimental error. The SERS intensity enhancement was consistently greater for the stereomatched complex (e.g., LC-LCGNP–LP) compared to the stereomismatched pair (e.g., LC-LCGNP–DP), as illustrated in Figure 3a,b. This preferential enhancement supports a model of more favorable binding due to better stereochemical complementarity and reduced steric hindrance in the matched system. To ensure statistical robustness of these intensity differences, 20 independent measurements were analyzed for key vibrational modes. Boxplots of the relative SERS intensities (Figure 3c; Figure S6b, Supporting Information) consistently showed higher intensities for stereomatched interactions (e.g., NH_2 stretching for LC-LP vs LC-DP), further supporting the phenomenon of stereoselective recognition mediated by the cysteine-functionalized CGNPs.

Additional validation of stereoselective capture was obtained from CD spectra of the supernatant and residue after incubating racemic phenylalanine with LC-LCGNPs, which showed enrichment of the unbound and bound enantiomers, respectively (Figure 3d). The residues thus represent LCGNP-bound fractions, while the supernatants contain the remaining unbound fractions. CD spectra of these fractions showed strong signals for enantiomers preferentially bound to their corresponding chiral CGNPs. LC-LCGNPs exhibited preferential binding to LP, as evidenced by the strong CD signal in the residue and the corresponding depletion of LP and presence of DP in the supernatant (Figure 3d). Quantitatively, the residue exhibited a degree of enrichment of 48.3%, confirming the highly selective capture of L-phenylalanine by the LC-LCGNP surface (detail in supporting information). Similarly, DC-LCGNPs selectively bound DP, with complementary trends observed in the residue and supernatant spectra (Figure S7a, Supporting Information). This result aligns seamlessly with SERS data, confirming that the enantioselectivity observed is driven by stereospecific ligand interactions and not merely plasmonic enhancement effects.

2.3.2. Binding Energetics and Structural Details from DFT Calculations

Density Functional Theory (DFT) calculations were performed to provide atomic-scale insights into the binding interactions and

energetics underpinning the observed enantioselectivity. Calculated binding energies and intermolecular distances revealed significant differences between stereochemically matched and mismatched complexes. For the L-cysteine and phenylalanine system, the LC–LP complex exhibited a favorable binding energy of -2.501 kcal/mol and a shorter average interaction distance (4.617 Å). In contrast, the mismatched LC–DP complex presented a higher binding energy (0.113 kcal/mol, indicative of weaker interaction or net repulsion) and a longer average interaction distance (4.989 Å) (Figure 5c). Similar trends were observed for D-cysteine interacting with DP (–2.112 kcal/mol, 4.383 Å) versus LP (0.113 kcal/mol, 5.079 Å) (Figure S7b, Supporting Information). Furthermore, the simulated Raman vibrational frequencies for the key modes (1446 cm^{-1}, 1404 cm^{-1}, 1341 cm^{-1}) align closely with experimentally observed SERS band positions and their shifts upon interaction (Figure S14, Supporting Information), corroborating the validity of this theoretical modeling.

2.3.3. Proposed Three-Point Interaction Mechanism

Integrating the spectroscopic observations and computational findings, a three-point interaction model,[7] commonly invoked for chiral recognition, is proposed for the cysteine-phenylalanine interaction at the CGNP surface (schematically illustrated in Figure 3a,b). The enantioselective recognition is attributed to complementary intermolecular interactions: primarily hydrogen bonds between the amino (NH_2) and carboxyl (COOH) groups of the surface-bound cysteine and the corresponding groups on phenylalanine, further stabilized by hydrophobic interactions between the cysteine side chain and the aromatic ring of phenylalanine. The specific spatial arrangement and chirality of these interacting groups dictate the stability and favorability of the complex. In addition to hydrogen bonding, electrostatic and steric effects, π–π stacking interactions, and van der Waals forces between the aromatic groups of phenylalanine and Chiral nanoparticle-bound cysteine could further influence molecular orientation and adsorption on the surface of CGNPs, potentially contributing to observed Raman shifts and enhanced enantioselectivity. While orientation-dependent Raman activity was not explicitly simulated, the compact and energetically favorable structures identified by DFT for stereomatched complexes likely facilitate an optimal orientation within the plasmonic fields, contributing to their higher observed SERS intensities.

2.3.4. Role of Nanoparticle Chirality and Polarization-Dependent Field Localization

To dissect the specific contribution of the CGNPs' intrinsic chirality to the observed plasmonic enhancement and enantiospecific SERS response, finite-difference time-domain (FDTD) simulations were conducted. The Raman enhancement factors (EF) for the 1004 cm^{-1} ring-breathing mode of D-phenylalanine (DP) were calculated (details in Supporting Information). LCGNPs exhibited an EF of 6.48×10^4, lower than that of achiral spherical gold nanoparticles (SGNPs, EF = 7.39×10^4), highlighting the superior chiral plasmonic enhancement capability of the chiral nanopropeller geometry (**Figure** 4h).

Further investigation focused on stereospecific SERS responses by comparing systems with matched versus mismatched chirality between the functionalized CGNP and the analyte. For instance, the homochiral pairing of LC-functionalized LCGNPs with LP (LC-LCGNPs–LP) exhibited approximately 30% greater Raman intensity at the characteristic phenylalanine band of 1348 cm^{-1} compared to a heterochiral system involving a D-chiral gold surface (e.g., LC-functionalized DCGNPs with LP, LC-DCGNPs–LP) (Figure 4a,d). The heterochiral system displayed weaker SERS responses, indicative of reduced adsorption efficiency and/or less effective plasmonic coupling due to stereomismatch (Figure 4a).

Quantitative comparisons using chiral discrimination ability (CDA), derived from relative Raman intensities (details in Figure S9, Supporting Information), further support these findings. CDA values were determined to be 5.56% for L-cysteine (LC) alone, 15.6% for LC-functionalized SGNPs (LC-SGNPs), and 36.0% for LC-LCGNPs. The modest stereoselectivity for LC alone is attributed to weak hydrogen-bonding. While SGNPs enhance signal intensity via surface plasmon resonance, their achiral nature limits enantioselectivity. In contrast, the significantly higher CDA for CGNPs underscores the critical role of their structurally encoded chirality in generating spatially asymmetric electromagnetic fields that selectively enhance interactions with one enantiomer. This CDA of 36.0% surpasses many values reported in the literature (**Table 1**).

FDTD simulations provided fundamental optical insights into these experimental observations by examining the influence of structural chirality on local electromagnetic field distributions under circularly polarized light (CPL) illumination. Achiral SGNPs, as expected, exhibited nearly identical field patterns under left- (LCP) and right-circularly polarized (RCP) light (Figure 4b), consistent with their lack of intrinsic chirality. Conversely, CGNPs displayed strongly polarization-dependent near-field enhancements (Figure 4c; Figure S11, Supporting Information). Specifically, LCGNPs illuminated with LCP (a matched handedness condition) demonstrated approximately 35% greater near-field intensity compared to DCGNPs under the same LCP illumination (a mismatched condition). This enhanced field confinement in matched systems arises from the effective alignment of the spin angular momentum (SAM) of the incident CPL with the intrinsic chirality of the nanopropellers, leading to more efficient plasmonic mode excitation and localization.[41]

Simulated optical spectra (scattering and absorption, Figure 4f; Figure S12b,c, Supporting Information) revealed that matched polarization-chirality conditions (e.g., LCP illuminating LCGNPs) selectively favored the excitation of radiative plasmonic modes. This was manifested by increased scattering intensity (6–19%) and reduced absorption (11–42%) compared to mismatched scenarios. These findings directly correlate with the experimentally observed SERS signal enhancement under matched chirality conditions (Figure 4a; Figure S8, Supporting Information), as radiative modes are more effective in enhancing Raman scattering through efficient photon-molecule coupling. Simulated extinction spectra (Figures S10,S12a, Supporting Information) further supported this, showing that under matched conditions, extinction was primarily driven by scattering, whereas mismatched conditions led to increased non-radiative absorption. This confirms that total extinction is

Table 1. Comparison of chiral sensing capabilities of various reported nanostructures and CGNPs.

Nanostructure	Enantioselectivity	Chiral Analyte	Refs.
D-DOPA-imprinted mesoporous Pt-Ir alloys	26%	3,4- dihydroxyphenylalanine	[11]
L-DOPA-imprinted mesoporous Pt-Ir alloys	27%	3,4- dihydroxyphenylalanine	[11]
S-Ag film	11%	Alanine	[26]
R-Ag film	20%	Alanine	[26]
D-Au with homochiral surface	28.3%	Tryptophan	[25]
L-Au with homochiral surface	32.7%	Tryptophan	[25]
TiO2/MIL-125NH-L-His NTs	33%	3,4- dihydroxyphenylalanine	[39]
160-D-PheOMe/Zn-TCPP	16.6%	Tryptophan	[40]
LC-LCGNPs	36%	Phenylalanine	This work

modulated by the SAM alignment between the incident light and the nanoparticle's chirality.[42]

Simulated energy density profiles (Figure 4g; Figure S12d, Supporting Information) provided spatial insight into these optical effects. LCGNPs under LCP illumination (matched) displayed broader, more delocalized energy density distributions, indicative of effective excitation of multiple plasmonic hotspots along the nanopropeller blades. In contrast, mismatched polarization scenarios (e.g., DCGNPs under LCP) resulted in weaker, spatially constrained fields. This polarization-dependent spatial energy distribution directly contributes to the experimental differences in SERS intensities observed between homochiral and heterochiral interactions.

Table 2 summarizes key simulated optical properties alongside experimental SERS enhancement data, reinforcing the relationship between structural chirality, CPL alignment, and plasmonic field enhancement. Under matched polarization conditions (LCP + LCGNPs and RCP + DCGNPs), calculated Raman Enhancement Factor (REF) values were substantially higher (2.68×10^4 and 1.93×10^4, respectively) compared to mismatched configurations (ca. 9×10^3). This quantitative agreement validates the FDTD model and underscores the decisive role of the CGNPs' structural chirality in optimizing plasmonic enhancement for SERS. The spherical gold nanoparticles (SGNPs) yield higher average Raman enhancement in the experiments under unpolarized excitation due to their isotropic plasmonic response, CGNPs are optimized for enantioselective enhancement. FDTD simulations (Figure 4b,c) clearly show that CGNPs generate significantly stronger near-field intensities when the handedness of the illumination matches the particle's geometry. This selective field amplification, though not fully reflected in bulk EF measurements in experiments (Figure 4h), is essential for stereospecific molecular recognition. Therefore, CGNPs are uniquely suited for chiral sensing applications, where polarization and molecular matching drive functional performance. The collective optical properties (scattering, absorbance, extinction) of LCGNPs and DCGNPs under LCP, alongside experimental EFs for chiral and achiral gold, are presented in Figure 4h, providing a robust mechanistic framework. These results align with theoretical predictions of optical chirality density by Tang and Cohen[41] and extend insights from planar chiral structures to solution-processable colloidal platforms.[41,43]

2.4. Quantitative Sensing Performance and Substrate Reusability

2.4.1. Determination of Enantiomeric Excess (ee%)

The capability of cysteine-functionalized CGNPs to quantify enantiomeric excess (ee%) was tested using racemic mixtures of L-phenylalanine (LP) and D-phenylalanine (DP) at varying molar ratios (detailed protocols in Supporting Information). **Figure 5a**

Table 2. Simulated optical properties of chiral gold nanopropellers (CGNPs) including the extinction, enhancement factor (EF), Raman Enhancement Factor, g-factor of L/D-CGNPs under circularly polarized (L/R-CP) illumination and the experimental SERS signal intensity for stereo-matching and mismatching interaction.

System (CGNPs—CP)	EF[a)]	REF[a)]	Ext[a)]. Peak [nm]	g-Fac.[a)]	Exp. SERS (CGNPs—P[a)]
L-CGNP + LCP	12.8	2.68×10^4	≈605	−0.06	Highest signal (Stereo-matching)
D-CGNP+ RCP	11.8	1.93×10^4	≈605	+0.06	Highest signal (Stereo-matching)
L-CGNP + RCP	9.82	9.23×10^3	Broader & less intense	≈0	Weaker signal (Stereo-mismatching)
D-CGNP + LCP	9.64	8.65×10^3	Broader & less intense	≈0	Weaker signal (Stereo-mismatching)

[a)] g-Fac: g-factor, Ext: extinction, EF: Enhancement factor, REF: Raman Enhancement Factor, P: enantiomer of Phenylalanine, CP: circularly polarized light, L/R-CP: left/right-handed-CP.

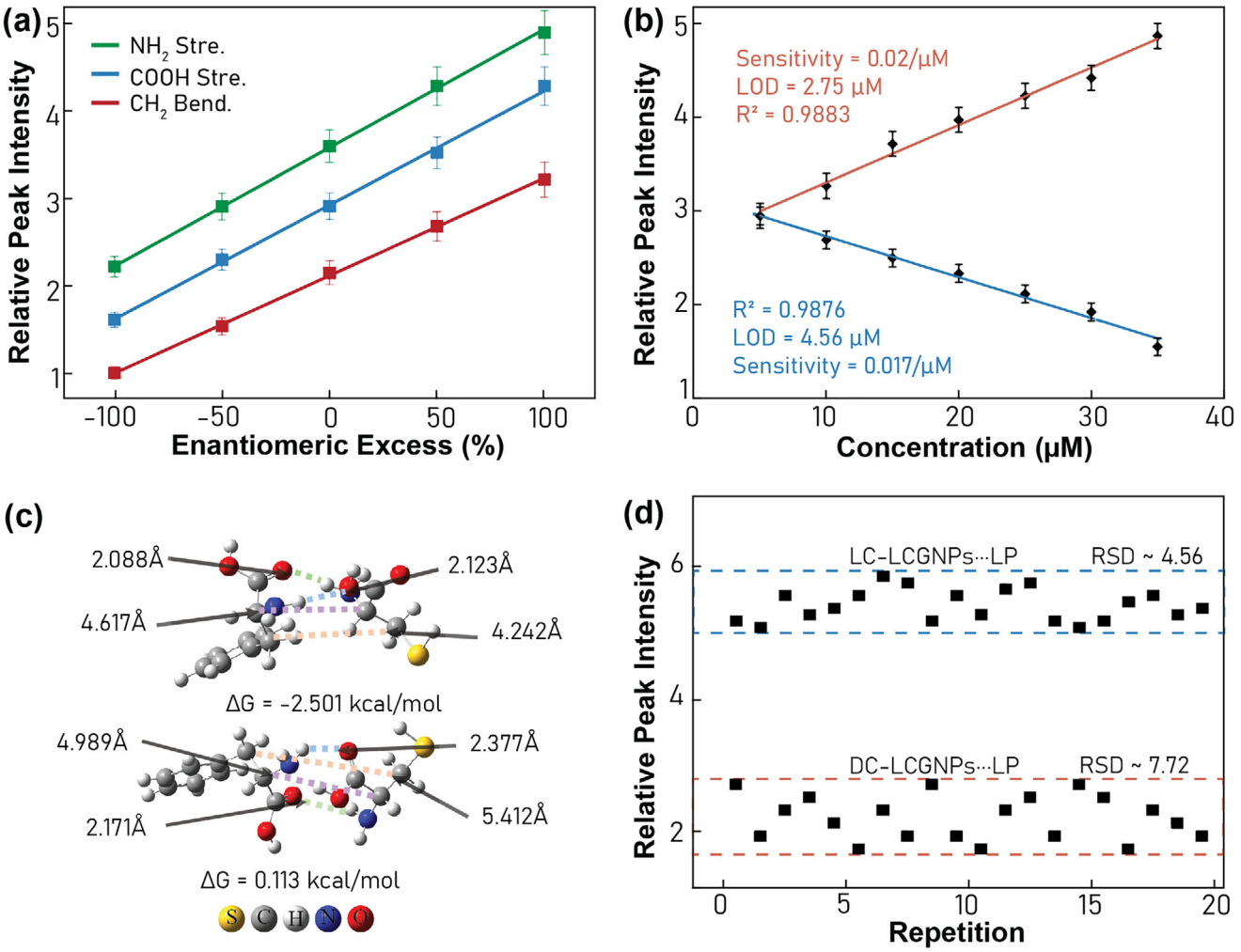

Figure 5. Performance metrics for quantitative chiral sensing. a) Linear calibration of relative SERS intensity vs. enantiomeric excess. b) SERS response curves across phenylalanine concentrations. c) Binding energy and geometry comparisons from DFT. d) Reusability test showing consistent signal across cycles and sampling positions.

illustrates the relationship between ee% and the relative SERS intensities of three prominent phenylalanine Raman bands: NH_2 stretching at 1348 cm^{-1}, COOH stretching at 1400 cm^{-1}, and CH_2 bending at 1427 cm^{-1}, respectively, in the phenylalanine mixture. The positive and negative *ee*% indicate a higher proportion of LP and a higher proportion of DP in the racemate of Phenylalanine, respectively. A clear linear relationship was observed between the relative SERS intensity of these bands and the ee%. For LC-functionalized LCGNPs, signal intensities progressively increased as the ee% shifted toward positive values (excess LP), while diminishing for negative ee% values (excess DP). Conversely, DC-functionalized CGNPs exhibited the opposite trend, with intensities increasing at higher DP concentrations (negative ee%), consistent with their enantioselective binding preferences (Figure S13, Supporting Information). These linear correlations demonstrate the platform's capacity for precise quantification of enantiomeric excess.

2.4.2. Sensitivity and Limit of Detection

The sensitivity of the CGNP platform was determined by varying the total phenylalanine concentration from 5 μM to 35 μM. For stereomatched systems (LC-functionalized LCGNPs with LP, and DC-functionalized LCGNPs with DP), SERS signal intensities at 1348 cm^{-1} exhibited a clear concentration-dependent enhancement (Figure 5b). Linear regression analysis showed excellent correlation ($R^2 = 0.9883$ for LC-LCGNP–LP, and $R^2 = 0.9849$ for DC-LCGNP–DP), confirming reliable analyte quantification. In contrast, mismatched host-guest interactions showed a decreasing trend in SERS intensity with increasing concentration of the mismatched enantiomer, as discussed previously.

The limit of detection (LOD), calculated based on signal-to-noise ratios (details in Supporting Information), was determined for these systems. Homochiral pairings (e.g., LC-LCGNPs–LP) achieved an LOD of 2.75 μM. This was substantially lower than

the LOD for opposite-handed pairings (e.g., LC-LCGNPs–DP), which was 4.56 μM (Figures 4e,5b). DC-functionalized LCGNPs demonstrated analogous trends, achieving LODs of 4.10 μM for homochiral pairing and 4.85 μM for heterochiral interactions (Figure S13, Supporting Information). These results highlight the enhanced sensitivity achieved through stereomatched interactions on the CGNP platform.

2.4.3. Substrate Stability and Reusability

The practical applicability of a SERS substrate is significantly influenced by its stability and reusability. The reusability of the cysteine-functionalized CGNP substrates was examined using a mild, pH-driven analyte recovery method.[44] Following recovery, the substrates were reused for SERS detection of phenylalanine enantiomers at a fixed concentration (0.1 M). Figure 5d presents the SERS intensities at 1348 cm^{-1} recorded across 20 random positions on the regenerated LC- and DC-functionalized LCGNP substrates. The relative standard deviation (RSD) values (indicated on each data set) remained consistently low, highlighting excellent reproducibility and minimal variability in signal intensity. This stability confirms that CGNP substrates retain their functional integrity and enantioselective sensing capability even after multiple recovery cycles, a critical factor for potential industrial or clinical adoption.

3. Conclusion

In this work, we have successfully designed and implemented cysteine-functionalized chiral gold nanopropellers (CGNPs) as an effective platform for enantioselective molecular recognition. Experimental SERS studies demonstrated that these CGNPs, when interacting with phenylalanine enantiomers, yield distinct spectral responses contingent upon stereochemical matching. Specifically, homochiral CGNP-analyte systems exhibited approximately 30% greater SERS intensity compared to heterochiral systems, enabling a quantitative chiral discrimination ability (CDA) of 36.0% and a detection limit for L-phenylalanine as low as 2.75 μM. Mechanistically, we show that optical field enhancement and molecular binding are not independent phenomena, but rather synergistically coupled through structural and chiral alignment. DFT calculations reveal favorable energetics and binding geometries in homochiral complexes, while FDTD simulations revealed that the intrinsic structural chirality of the CGNPs, when coupled with appropriately handed circularly polarized light, generates enhanced and asymmetrically localized electromagnetic near-fields, particularly promoting radiative plasmon modes.

The significance of these findings lies in the demonstration of a dual-modality approach where both engineered plasmonic chirality at the nanoscale and specific molecular binding events cooperatively enhance enantioselectivity. The CGNP platform's performance, particularly its CDA, surpasses that of many existing SERS-based chiral sensing systems, highlighting the efficacy of the nanopropeller morphology in creating potent chiral optical environments. Furthermore, the detailed elucidation of how structural chirality influences local field distributions and couples with molecular interactions provides valuable insights for the rational design of advanced optical materials with tailored chiroptical responses. The demonstrated stability and reusability of the CGNP substrates further underscore their potential for practical applications.

Looking forward, the design principles and mechanistic understanding established here offer a robust foundation for extending this chiral sensing strategy to a broader range of chiral molecules critical in pharmaceutical development, biological studies, and catalysis. Future research could focus on optimizing the CGNP geometry and surface chemistry for even greater sensitivity and selectivity, or for targeting specific classes of analytes. The integration of these CGNPs into microfluidic systems or portable SERS devices could pave the way for high-throughput screening and real-world, on-site chiral analysis. Moreover, the demonstrated control over chiral light-matter interactions at the CGNP surface opens avenues for exploring their utility in other chiroptical applications, such as enantioselective catalysis driven by chiral plasmonic fields or the development of novel circular polarization-sensitive photodetectors and optical switches. Ultimately, this work contributes to the evolving field of chiral nanophotonics, aiming to translate sophisticated control over nanoscale optical chirality into functional and impactful technologies.

4. Experimental Section

Chemicals: L-Phenylalanine (99% purity), D-phenylalanine (99% purity), L-cysteine (>98% purity), and D-cysteine (>98% purity) were procured from Shanghai Titan Scientific Co., Ltd. L-glutathione (L-GSH, ≥98%), cetyltrimethylammonium bromide (CTAB, ≥99%), and L-ascorbic acid (AA, ≥99%) were obtained from Sigma-Aldrich. D-glutathione (D-GSH, ≥96%) was purchased from GL Biochem Ltd. Spherical gold nanoparticles (for comparative EF calculations) were sourced from Shanghai Macklin Biochemical Co., Ltd. All chemical reagents were utilized as received without additional purification. Deionized water (Sigma-Aldrich) was used for all solution preparations.

Synthesis of Chiral Gold Nanopropellers (CGNPs): CGNPs were prepared by a seed-mediated growth approach, employing gold decahedra seeds and L- or D-glutathione as chiral directing agents.[24] Gold decahedra seeds were synthesized separately and stored in 1.0 mM cetyltrimethylammonium bromide (CTAB) solution at room temperature. For nanopropeller formation, a growth solution containing $HAuCl_4$ (0.37 mM), CTAB (14.75 mM), ascorbic acid (8.8 mM) as reducing agent, and L/D-glutathione (3.6 μM) was prepared. The reaction was initiated by adding 2.0 μL of the seed solution into 5 mL of the growth solution and and allowing it to proceed under static conditions at 30 °C. The growth proceeded for 2 hours, during which the solution color transitioned from purplish red to bluish red, and ultimately to pinkish gray, indicating successful nanoparticle anisotropic growth. The nanoparticles were isolated by centrifugation at 4,500 rpm for 3 minutes and subsequently purified by washing three times with ultrapure water for subsequent characterization. The purified CGNPs were dispersed in 1 mM CTAB solution, stored at room temperature, and their long-term colloidal stability was evaluated by UV–vis spectroscopy.

Surface Functionalization of CGNPs with Cysteine: Functionalization of CGNPs was carried out following a procedure adapted from the literature[45] to ensure thorough modification and high purity. A 5 mL aliquot of 0.5 mM CGNP solution was mixed with 250 μL of 0.1 mM L-cysteine or D-cysteine under continuous stirring for 2 hours. The functionalized nanoparticles were purified by centrifugation at 10,000 rpm for 30 minutes, followed by three washing cycles with ultrapure water to remove unbound cysteine. The purified nanoparticles were dispersed in water using sonication, yielding LC-CGNPs (L-cysteine-functionalized CGNPs) and

DC-CGNPs (D-cysteine-functionalized CGNPs). Both LC-CGNPs and DC-CGNPs were stored at room temperature for subsequent analysis.

Raman Spectroscopy and SERS Measurements: Raman and SERS measurements were performed using a WITec alpha300 confocal Raman spectrometer equipped with a 532 nm He-Ne laser excitation source operating at a power of 12 mW. A 600 gr/mm grating was utilized for spectral dispersion and detection. For SERS analysis, suspensions of functionalized CGNPs were drop-cast onto clean high-purity quartz slides and allowed to dry at room temperature, forming SERS-active substrates. To evaluate chiral recognition, these CGNP substrates (e.g., LC-LCGNPs, DC-LCGNPs – ensure these specific combinations used in experiments were consistently named) were incubated with 0.1 mM solutions of D-phenylalanine (DP) or L-phenylalanine (LP) for 30 minutes under gentle stirring to ensure adequate binding interactions and system equilibration. Raman spectra were then collected from the resulting CGNP-analyte complexes using a 50× objective lens. Multiple spectra were acquired from different spots on each sample to ensure reproducibility. Direct interpretation of Raman spectra was often complicated by spectral artifacts, therefore, the relative peak intensities, normalized to the Raman band at 1292 cm^{-1} (C-C vibrations), were used to ensure reliability and consistency data. All SERS experiments were replicated with at least three independently synthesized batches of CGNPs to ensure reproducibility and the robustness of the synthesis and sensing methodology.

Circular Dichroism (CD) Spectroscopy: CD spectra were acquired using a Circular Dichroism Spectrometer V100 (Rudolph Research Analytical, Autopol IV-T) equipped with a 100 mm path-length quartz cuvette (outer dimensions: 45 mm x 12.5 mm x 3.5 mm). Data were collected in the 200–800 nm spectral range with a step size of 1 nm and an integration time of 0.5 s per point.

Density Functional Theory (DFT) Calculations: DFT calculations were performed using Gaussian 16 software[46] to investigate the interactions between L-cysteine or D-cysteine and the phenylalanine enantiomers. The B3LYP functional was employed with the 6-311G(d,p) basis set. Grimme's D3 dispersion correction was included to account for van der Waals interactions. Geometry optimizations were conducted in the gas phase, and all optimized structures were confirmed as true minima by frequency calculations (no imaginary frequencies). Intermolecular distances and hydrogen bonding patterns were analyzed from the optimized geometries. Interaction energies were calculated and corrected for basis set superposition error (BSSE) using the counterpoise method.

Finite Difference Time Domain (FDTD) Simulations: Three-dimensional FDTD simulations were performed using Lumerical FDTD Solutions to investigate the optical properties of the CGNPs and the origin of enantioselective enhancements. The models comprised D- and L-type CGNPs (based on SEM dimensions) immersed in a homogeneous medium with a refractive index of $n = 1.33$ (approximating water). Illumination was simulated using a circularly polarized plane wave (generated by phase-shifting Ex and Ey components) under a total-field scattered-field (TFSF) source. Both spectral (500–700 nm) and narrowband (centered at 532 nm for SERS excitation) simulations were conducted. A fine spatial mesh (mesh override: 1.5 nm) was employed in the vicinity of the nanoparticles, with a total simulation time of 1000 fs and perfectly matched layer (PML) absorbing boundaries. Various monitors were used to capture near-field intensity distributions (|E|2), far-field energy density, extinction, scattering, and absorption spectra, as well as CD signals and g-factors.

Supporting Information

Supporting Information is available from the Wiley Online Library or from the author.

Acknowledgements

This work was financially supported by the Center of Synthetic Biology and Integrated Bioengineering of Westlake University (Project No. WU2024A006), as well as the provision of instrumental facilities by Westlake University. The authors thanks to Dr. Zhong CHEN and Dr. Yuan CHENG from Instrumentation and Service Center for Molecular Sciences at Westlake University for the assistance in experimental measurements.

Conflict of Interest

The authors declare no conflict of interest.

Data Availability Statement

The data that support the findings of this study are available from the corresponding author upon reasonable request.

Keywords

chiral gold nanoparticle, chirality, enantioselectivity, nanopropellers, SERS

Received: May 18, 2025
Revised: July 26, 2025
Published online: September 8, 2025

[1] A. J. Callahan, S. Gandhesiri, T. L. Travaline, R. M. Reja, L. L. Salazar, S. Hanna, Y.-C. Lee, K. Li, O. S. Tokareva, J.-M. Swiecicki, *Nat. Commun.* **2024**, *15*, 1813.
[2] Y. Xu, T. F. Zhu, *Science* **2022**, *378*, 405.
[3] M. Melchert, A. List, *Int. J. Biochem. Cell Biol.* **2007**, *39*, 1489.
[4] E. Tokunaga, T. Yamamoto, E. Ito, N. Shibata, *Sci. Rep.* **2018**, *8*, 17131.
[5] H. Yu, X. Yong, J. Liang, J. Deng, Y. Wu, *Ind. Eng. Chem. Res.* **2016**, *55*, 6037.
[6] Y. Okamoto, T. Ikai, *Chem. Soc. Rev.* **2008**, *37*, 2593.
[7] P. Dwivedi, C. Wu, L. M. Matz, B. H. Clowers, W. F. Siems, H. H. Hill, *Anal. Chem.* **2006**, *78*, 8200.
[8] J. Labuta, S. Ishihara, T. Šikorský, Z. Futera, A. Shundo, L. Hanyková, J. V. Burda, K. Ariga, J. P. Hill, *Nat. Commun.* **2013**, *4*, 2188.
[9] D. Parker, *Chem. Rev.* **1991**, *91*, 1441.
[10] J. Liu, H. Zhou, W. Yang, K. Ariga, *Acc. Chem. Res.* **2020**, *53*, 644.
[11] S. Butcha, S. Assavapanumat, S. Ittisanronnachai, V. Lapeyre, C. Wattanakit, A. Kuhn, *Nat. Commun.* **2021**, *12*, 1314.
[12] M. Haroon, I. Abdulazeez, T. A. Saleh, A. A. Al-Saadi, *Electrochim. Acta* **2021**, *387*, 138463.
[13] X. You, C.-W. Huang, K. Vinodgopal, J. M. Atkin, *J. Chem. Phys.* **2024**, *161*, 094204.
[14] X. You, S. Maharjan, K. Vinodgopal, J. M. Atkin, *Phys. Chem. Chem. Phys.* **2024**, *26*, 9871.
[15] W. Ding, Y. Xia, H. Song, T. Li, D. Yang, A. Dong, *Angew. Chem.* **2024**, *136*, 202401945.
[16] M. Arabi, A. Ostovan, Y. Wang, R. Mei, L. Fu, J. Li, X. Wang, L. Chen, *Nat. Commun.* **2022**, *13*, 5757.
[17] X. Gao, B. Han, X. Yang, Z. Tang, *J. Am. Chem. Soc.* **2019**, *141*, 13700.
[18] X. Xiao, C. Chen, Y. Zhang, H. Kong, R. An, S. Li, W. Liu, Q. Ji, *Angew. Chem.* **2021**, *133*, 25232.
[19] T.-H. Xiao, Z. Cheng, Z. Luo, A. Isozaki, K. Hiramatsu, T. Itoh, M. Nomura, S. Iwamoto, K. Goda, *Nat. Commun.* **2021**, *12*, 3062.
[20] Y. Shi, J. Liu, J. Xin, B. Han, Y. Zhang, J.-J. Wang, *ACS Appl. Polym. Mater* **2024**, *6*, 9039.
[21] W. Songmeng, Y.-F. Wang, L. Huang, L.-S. Zheng, H. Nian, Y.-T. Zheng, H. Yao, W. Jiang, X. Wang, L.-P. Yang, Chiral Recognition of Neutral Guests by Chiral Naphthotubes with a Bis-thiourea Endo-Functionalized Cavity **2023**.

[22] A. Skvortsova, J. H. Han, A. Tosovska, P. Bainova, R. M. Kim, V. Burtsev, M. Erzina, P. Fitl, M. Urbanova, V. Svorcik, *ACS Appl. Mater. Interfaces* **2024**, *16*, 48526.
[23] G. Palermo, M. Rippa, D. M. Aceti, A. Guglielmelli, L. Valente, D. Sagnelli, A. D'Avino, B. Guilcapi, N. Maccaferri, L. Petti, G. Strangi, *Nano Lett.* **2024**, *24*, 10202.
[24] Y. Zheng, X. Li, L. Huang, X. Li, S. Yang, Q. Wang, J. Du, Y. Wang, W. Ding, B. Gao, *J. Am. Chem. Soc.* **2023**, *146*, 410.
[25] F. Wu, Y. Tian, X. Luan, X. Lv, F. Li, G. Xu, W. Niu, *Nano Lett.* **2022**, *22*, 2915.
[26] L. Ma, Y. Cao, Y. Duan, L. Han, S. Che, *Angew. Chem., Int. Ed.* **2017**, *56*, 8657.
[27] H. Kim, S. W. Im, N. H. Cho, D. H. Seo, R. M. Kim, Y. C. Lim, H. E. Lee, H. Y. Ahn, K. T. Nam, *Angew. Chem.* **2020**, *132*, 13076.
[28] F. Wu, F. Li, Y. Tian, X. Lv, X. Luan, G. Xu, W. Niu, *Nano Lett.* **2023**, *23*, 8233.
[29] L. A. Warning, A. R. Miandashti, L. A. McCarthy, Q. Zhang, C. F. Landes, S. Link, *ACS Nano* **2021**, *15*, 15538.
[30] X. Sun, N. Wang, Y. He, H. Kong, H. Yang, X. Liu, *J. Mater. Chem. B* **2021**, *9*, 7167.
[31] S. Zhou, J. Guo, Z. Dai, C. Liu, J. Zhao, Z. Gao, Y.-Y. Song, Engineering Homochiral MOFs in TiO2 Nanotubes as Enantioselective Photoelectrochemical Electrode for Chiral Recognition **2021**.
[32] Q. Zhao, H. Hilal, J. Kim, W. Park, M. Haddadnezhad, J. Lee, W. Park, J.-W. Lee, S. Lee, I. Jung, *J. Am. Chem. Soc.* **2022**, *144*, 13285.
[33] Y. Tang, A. E. Cohen, *Phys. Rev. Lett.* **2010**, *104*, 163901.
[34] J. Zheng, C. Boukouvala, G. R. Lewis, Y. Ma, Y. Chen, E. Ringe, L. Shao, Z. Huang, J. Wang, *Nat. Commun.* **2023**, *14*, 3783.
[35] J. Wan, L. Sun, X. Sun, C. Liu, G. Yang, B. Zhang, Y. Tao, Y. Yang, Q. Zhang, *J. Am. Chem. Soc.* **2024**, *146*, 10640.
[36] L. Zhang, Y. Chen, J. Zheng, G. R. Lewis, X. Xia, E. Ringe, W. Zhang, J. Wang, *Angew. Chem.* **2023**, *135*, 202312615.
[37] G. Yao, Q. Huang, *J. Phys. Chem. C* **2018**, *122*, 15241.
[38] S. Wang, X. Liu, S. Mourdikoudis, J. Chen, W. Fu, Z. Sofer, Y. Zhang, S. Zhang, G. Zheng, *ACS Nano* **2022**, *16*, 19789.
[39] S. Zhou, J. Guo, Z. Dai, C. Liu, J. Zhao, Z. Gao, Y.-Y. Song, *Anal. Chem.* **2021**, *93*, 12067.
[40] N. Liu, J. Li, W. Cai, D. Wu, Y. Kong, *Anal. Chem.* **2023**.
[41] Y. Chen, J. Zheng, L. Zhang, S. Li, Y. Chen, K. K. Chui, W. Zhang, L. Shao, J. Wang, *ACS Nano* **2023**, *18*, 383.
[42] S. K. Chaubey, R. Kumar, P. L. Lalaguna, M. Kartau, S. Bianco, V. Tabouillot, A. R. Thomson, A. Sutherland, O. Lyutakov, N. Gadegaard, *Small* **2024**, *20*, 2404536.
[43] Y. Lin, H. Chai, L. Fan, D. Che, X. Liu, J. Wang, *J. Phys. Chem. C* **2024**, *128*, 7698.
[44] S. Chakraborty, C. L. Kitchens, *J. Phys. Chem. C* **2019**, *123*, 26450.
[45] Y. Zhang, J. Liu, D. Li, X. Dai, F. Yan, X. A. Conlan, R. Zhou, C. J. Barrow, J. He, X. Wang, *ACS Nano* **2016**, *10*, 5096.
[46] M. Frisch, G. Trucks, H. Schlegel, G. Scuseria, M. Robb, J. Cheeseman, G. Scalmani, V. Barone, G. Petersson, H. Nakatsuji, in *Gaussian 16 Revision C. 01*, Gaussian Inc, Wallingford CT **2016**, Vol. *1*, p. 572.